nature geoscience

Article

https://doi.org/10.1038/s41561-026-02018-w

Negative core–mantle boundary heat flux beneath low-shear-wave-velocity provinces

Received: 31 December 2025

Accepted: 15 May 2026

Published online: 17 June 2026

Check for updates

Frédéric Deschamps[1] ✉, Joshua Martin Guerrero[1], Hagay Amit[2], Filipe Terra-Nova[3] & Wen-Pin Hsieh[1]

The Earth's core–mantle boundary hosts structures and processes that affect our planet's thermal evolution. Spatial and temporal changes in core–mantle boundary heat flux influence core dynamics and its associated geodynamo. These variations, in turn, are controlled by details of mantle dynamics and may be affected by lowermost mantle structures, in particular large low-shear-wave-velocity provinces, which are commonly interpreted as reservoirs of hot, chemically differentiated material. Here we perform simulations of mantle thermochemical convection that account for changes in thermal conductivity with temperature and for excess heating in piles of dense material, modelling large low-shear-wave-velocity provinces. We show that beneath these piles, heat flux can be locally negative, that is, heat flows to the core. In addition, heat flux remains lower than the adiabatic core heat flux throughout the piles base, while slab arrival at the core–mantle boundary triggers high heat flux spikes, increasing lateral heat flux heterogeneity. Our findings support the hypothesis that regional stratification occurs at the top of the core, reconciling present-day geomagnetic and seismic observations in this region. At timescales of 100 Myr, locally negative heat flux may explain the onset and termination of long periods without geomagnetic field polarity reversals known as superchrons.

Spatial and temporal variations in the Earth's core–mantle boundary (CMB) heat flux, Φ_{CMB}, strongly influence the dynamics of the outer core and the generation of the Earth's magnetic field through the geodynamo process. On timescales shorter than the mantle advection time, lateral heterogeneities in Φ_{CMB} may prescribe preferred locations of intense geomagnetic flux patches at the top of the core[1], outer core convection and inner core growth pattern[2] and recurrent sites of weak field intensity at Earth's surface[3]. In addition, core convection simulations with CMB heat flux heterogeneity accommodating regional subadiabatic conditions[4,5] may reconcile seismic evidence in favour of stratification at the top of the core[6] and geomagnetic evidence against it[7,8]. On much longer timescales, temporal changes in Φ_{CMB} amplitude and pattern may explain the enigmatic variability in magnetic polarity reversal frequency, including superchrons and hyper-frequency reversals[9–13]. A good understanding of these phenomena requires precise knowledge of changes in Φ_{CMB} with space and time, and of the processes controlling these variations. On the mantle side, the CMB region is the final destination of subducted slabs[14,15] and further hosts seismic structures whose exact nature and origin are not yet fully understood. These include the D″ discontinuity, which is thought to be the seismic signature of the phase change from bridgmanite to postperovskite (pPv)[16,17]; the ultralow velocity zones (ULVZ)[18], potentially related to partially molten or very high-density patches; and the continental-scale large low-shear-wave-velocity provinces (LLSVPs) located beneath Africa and the Pacific[19], whose structure might be more complex than previously thought[20,21] and which are best explained by hot, chemically differentiated material, possibly enriched in iron[22,23]. These structures impact deep mantle chemistry, dynamics and evolution and may further be involved in core–mantle interactions. In particular, lateral temperature variations above the CMB associated with slabs and LLSVPs

[1]Institute of Earth Sciences, Academia Sinica, Nangang, Taiwan. [2]Laboratoire de Planétologie et Géosciences, CNRS UMR 6112, Nantes Université, Univ Angers, Le Mans Université, Nantes, France. [3]Institut de Physique du Globe de Paris, Université Paris Cité, CNRS, Paris, France. ✉e-mail: frederic@earth.sinica.edu.tw

https://doi.org/10.1038/s41561-026-02018-w

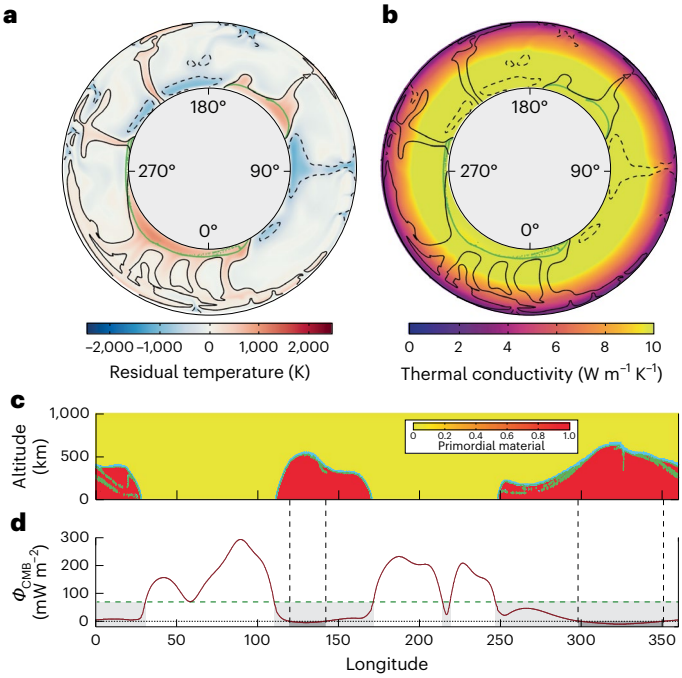

Fig. 1 | Snapshot of a simulation featuring negative CMB heat flux patches. Thermal conductivity temperature exponent is $a = 0.3$ and piles excess heating ratio is $R_H = 15$. **a**, Residual temperature. **b**, Thermal conductivity. **c**, Fraction of dense primordial material (colour code) in the bottom 1,000 km, showing piles of dense material. **d**, CMB heat flux as a function of longitude. In **a** and **b**, the plain and dashed black contours represent the boundaries of plumes and downwellings (Methods), respectively, and the green contours show the piles roof. In **c**, the spherical annulus is projected on a two-dimensional Cartesian grid, and the cyan contours indicate isolines of the composition with an interval of 0.1. In **d**, the dashed green line indicates the core adiabatic heat flux, Φ^{core}_{adia}, assuming an adiabatic gradient of 1 K km^{-1} and a core conductivity of 70 W m^{-1} K^{-1}, and the light- and dark-grey areas show the lateral extensions of regions with heat flux lower than Φ^{core}_{adia} and with negative heat flux, respectively.

induce variations in Φ_{CMB}, with cold (hot) regions being associated with locally high (low) heat flux, a trend that is amplified by variations of thermal conductivity with temperature[24,25]. Furthermore, due to their assumed formation process, either by accumulation of oceanic crust, relics of the Moon-forming giant impact[26] or the final stage of a basal magma ocean crystallization[27], LLSVPs are potentially enriched in heat-producing elements[28] (HPE), which would elevate their temperature. Both a temperature-dependent mantle thermal conductivity and excess HPE in LLSVPs may then strongly impact mantle dynamics, CMB heat flux and core dynamics. We investigate these effects by performing numerical simulations of whole-mantle thermochemical convection using the finite volume code StagYY[29] and show that Φ_{CMB} is not only lower than adiabatic core heat flux throughout LLSVPs but strikingly may be locally negative.

Numerical simulations of thermochemical convection

The numerical set-up we used is similar to that in ref. 30, except that the grid resolution (2,048 × 256 nodes) is finer (Methods). Simulations are conducted in spherical annulus[31], equivalent to two-dimensional slices bisecting a sphere at its equator, with isothermal, stress-free boundaries and assuming a compressible fluid. Thermal conductivity pressure dependence is taken from high-pressure mineral physics experiments[32–34], and its temperature dependence follows a $1/T^a$ trend. For lower mantle minerals, the exponent a is estimated in the range 0.25–0.5 (refs. 24,25,35–37). Here, we considered values between 0.0 (no temperature dependence) and 1.0. We fixed the total internally generated power to 11 TW (ref. 38) and modelled LLSVPs excess heating with the dense-to-regular material heating ratio, R_H (Methods), testing values of R_H up to 50, in agreement with estimates of LLSVPs enrichment in HPE[39]. Figure 1a,b shows residual temperature and thermal conductivity for a snapshot taken at the end of a simulation (see Extended Data Figs. 1 and 2 for other simulations). In all cases, we observe two to four piles of dense, hot material above the CMB, on top of which thermal plumes are being generated. Piles are separated by downwellings that push them and constrain their locations and sizes. Overall, more piles form at high R_H (≥30), whereas a has no influence on the number and size of piles. These structures are representative of the thermochemical distributions observed during the quasi-stationary phase (Supplementary Movies 1–4). During this phase piles may however slowly drift, split or merge, modifying their shape and altitude. Except for cases with $a = 1.0$ and $R_H \geq 10$, the density excess we prescribed, 140 kg m^{-3}, ensures that they remain overall stable and experience limited dragging from the plumes generated at their top. Because the mantle total heating rate is fixed, internal heating in the regular mantle decreases with increasing R_H (Methods), resulting in lower mantle average temperatures (Extended Data Fig. 3). Conductivity temperature dependence leaves mantle average temperature unaffected but strongly reduces thermal conductivity in the CMB region and lowers it further within piles (Extended Data Fig. 3). In addition, the r.m.s. in positive and negative temperature anomalies in the lowermost mantle (defined as the bottom 200 km) get stronger with increasing temperature dependence (Extended Data Fig. 4). These two properties strongly alter heat transfer at the CMB by reducing the mean Φ_{CMB} and by increasing its spatial heterogeneity.

Impact on CMB heat flux

Due to thermal conductivity reduction, the mean CMB heat flux, $<\Phi_{CMB}>$, sharply decreases with increasing temperature dependence (Fig. 2a,b). Time-averaged $<\Phi_{CMB}>$ drops from ~135 mW m^{-2} for $a = 0.0$ to ~20 mW m^{-2} for $a = 1.0$. Interestingly, for temperature dependence expected for Earth's mantle minerals ($0.2 \leq a \leq 0.5$) our simulations predict $<\Phi_{CMB}>$ well within the Earth's estimated range (25–110 mW m^{-2})[38]. By contrast, piles excess heating does not substantially influence $<\Phi_{CMB}>$ and only triggers moderate dispersion (especially at weaker temperature dependence). Time variations in $<\Phi_{CMB}>$ are limited, with a peak-to-peak amplitude ~20% of time-averaged $<\Phi_{CMB}>$ (Extended Data Fig. 5a), in agreement with variations predicted by models of convection that incorporate plate tectonics reconstruction[40]. Heat flux spatial heterogeneity, $\delta\Phi$ (Methods and Fig. 2c,d), is large even for constant conductivity ($\delta\Phi = 1.5$) and increases with temperature-dependent conductivity, up to ~3.0 for $a = 1.0$. Our simulations further indicate that time variations in $\delta\Phi$ are large with peak-to-peak amplitude >0.5, that is, 20–50% of the time-averaged values (Extended Data Fig. 5b). Time variations in $\delta\Phi$ are controlled by variations in the maximum heat flux, Φ_{max} (Extended Data Fig. 6), which are themselves controlled by the arrival and evolution of downwellings (see below). In contrast, the minimum heat flux, Φ_{min}, is related to the evolution of piles and varies on a much longer timescale.

Lateral variations in Φ_{CMB} (Fig. 1d and Extended Data Fig. 7) show two additional properties that may strongly impact core dynamics. First, Φ_{CMB} remains low (<10 mW m^{-2}) throughout piles of dense material and sharply decreases on their edges, triggering wide regions of low heat flux, possibly lower than the core adiabatic heat flux, Φ^{core}_{adia}. Fixing Φ^{core}_{adia} to 70 mW m^{-2} on the basis of recent estimates of core thermal conductivity[41], our simulations indicate that Φ_{CMB} is lower than Φ^{core}_{adia} throughout the piles of dense material and on their edges. For this value of Φ^{core}_{adia}, $<\Phi_{CMB}>$ is subadiabatic for all cases with $a > 0.4$, such that these cases may not explain the geodynamo. The extent of 'subadiabatic' regions depends on a and R_H and further varies with time but covers the entire piles in most cases (Extended Data Fig. 7). Average heat flux within subadiabatic regions, $<\Phi_{subadia}>$, varies again with a and

https://doi.org/10.1038/s41561-026-02018-w

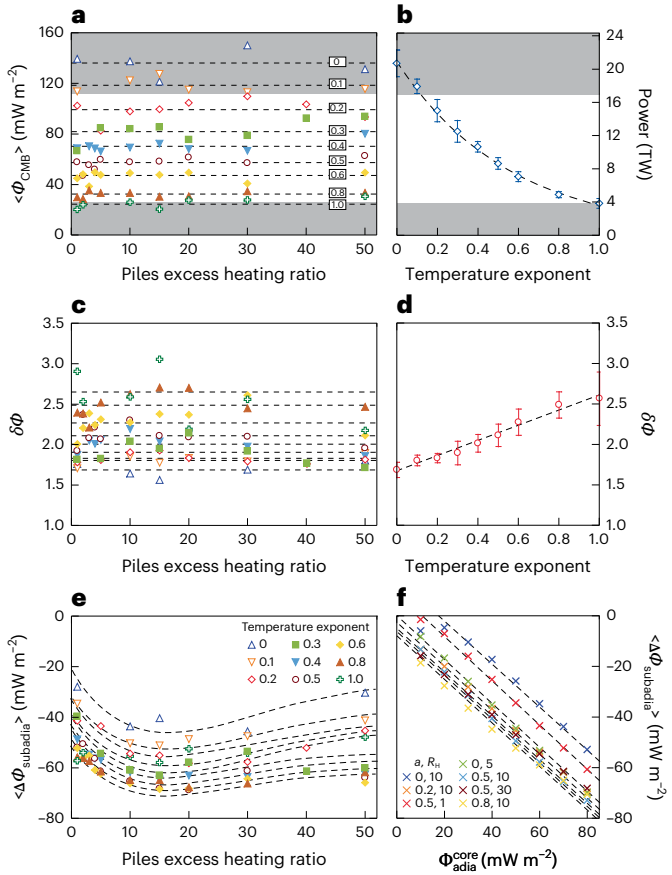

Fig. 2 | Time-averaged CMB heat flux statistics. a,**b**, Mean CMB heat flux, $<\Phi_{CMB}>$. **c**,**d**, Heat flux heterogeneity, $\delta\Phi$. **e**,**f**, Average residual subadiabatic heat flux, $<\Delta\Phi_{subadia}>$, defined as the difference between the average heat flux in subadiabatic regions and the core adiabatic heat flux, Φ^{core}_{adia}, here fixed to 70 mW m^{-2}. In **a**, **c** and **e**, data are plotted as a function of the thermochemical piles excess heating, R_H, and for different exponent of the thermal conductivity temperature dependence, a (symbols). In **b** and **d**, data are plotted as a function of the temperature exponent, a. The horizontal dashed lines in **a** and **c**, in descending order, indicate the conductivity's temperature exponent value and their corresponding mean heat flux value. The dashed curves in **e** correspond to a trend spline fitting the average residual subadiabatic heat flux. The dashed lines in **f** correspond to a linear trend in adiabatic heat flux and average residual subadiabatic heat flux. The shaded grey areas in **a** and **b** indicate the heat flux values outside the estimate of core power from ref. 38. In **b** and **d**, data are further averaged out over all the values of R_H (five to ten samples, depending on a), and the bars indicate one standard deviation and are represented as a function of the temperature exponent a. Panel **f** shows $<\Delta\Phi_{subadia}>$ as a function of Φ^{core}_{adia} and for selected simulations (symbols). Data are averaged over the last 2 Gyr of simulations.

R_H but levels off for R_H larger than ~20 (Fig. 2e). Interestingly, heat flux beneath piles is sufficiently low (<10 mW m^{-2}) to keep these regions subadiabatic for values of Φ^{core}_{adia} down to ~10 mW m^{-2} (Fig. 2f). This suggests that, in the Earth, CMB heat flux is most likely lower than the core adiabatic heat flux beneath LLSVPs.

Second, our simulations clearly show that heat flux highs are associated with slabs arrival at or spreading on the CMB (Fig. 3). Slab material is coldest as it reaches the CMB and then warms up as it spreads laterally. Consequently, highest values of Φ_{CMB} are observed where slabs hit (or have recently hit) the CMB (for example, at longitude 90° in Fig. 1), whereas older slabs induce secondary but still strong peaks (for example, between longitudes 180° and 200° in Fig. 1). In our simulations, two to five slabs are simultaneously observed at any given time, with the number of slabs increasing with R_H. Although slabs are not synchronous (they do not necessarily reach the CMB at the same time), we note that the time sequences in maximum Φ_{CMB} are strongly anticorrelated with the volume of slabs in the lowermost mantle and with the mean temperature within these regions (Fig. 3c–e), suggesting that both high heat flux spikes and strong heat flux heterogeneity (Fig. 3f) are triggered by slabs impacts on CMB. Likewise, simultaneous arrivals of two or more slabs at different locations may result in exceptionally high heat flux spikes.

Patches of negative CMB heat flux

A key result revealed by our simulations is the formation of regions where Φ_{CMB} is negative, that is, heat is flowing from the mantle to the core. These patches of negative heat flux result from local negative temperature gradient at the bottom of the mantle and appear within piles of dense, hot material (Fig. 1c,d and Extended Data Fig. 7). Because piles are heated both from the core and from their interior and cooled by the plumes that form at their top, both the excess internal heating and the variations in thermal conductivity play a role in their thermal evolution and, thus, on the appearance of negative heat flux patches. Excess internal heating elevates the piles temperature and reduces the amount of heat that can be extracted from the core. A decrease in conductivity, due either to a higher temperature[24] or an enrichment in iron[32,33], also reduces the amount of heat that can be extracted from the core but, in addition, reduces heat extraction by plumes from the piles, slowing down their cooling. As a consequence, increases in the excess internal heating and the temperature dependence of conductivity should favour piles warming and the appearance of patches of negative Φ_{CMB}.

Our simulations confirm these trends but also point out a more complex behaviour (Fig. 4). Importantly, the formation of negative heat flux patches requires both an excess heating ratio $R_H \geq 2$ and a conductivity temperature dependence exponent $a \geq 0.1$ (Fig. 4a). Negative patches do not form if one of these conditions is not realized. Second, as one would expect, the excess heating needed to form piles decreases with increasing conductivity temperature dependence. Up to $a = 0.8$ and given the excess heating, a stronger temperature dependence leads to a larger amount of heat flowing to the core (Fig. 4b). For stronger temperature dependence, piles are less stable and the temperature increase is overcompensated by the decrease in conductivity, limiting heat exchange between the core and the mantle. Such large temperature dependences may however not apply to Earth's mantle minerals. The detailed influence of piles excess heating is less intuitive. At low temperature dependence ($a \leq 0.25$) patches are not anymore forming if R_H gets larger than some critical value, which, for $a = 0.2$, is around 40 (Fig. 4a). Additional simulations with $R_H = 100$, do not feature patches for $a = 0.3$ but still do for $a = 0.5$, suggesting that there is an upper limit in excess heating for the formation of patches, whose value increases with a. For a given temperature dependence, we further observe that the total amount of heat flowing to the core (Fig. 3b) and the average piles temperature (Extended Data Fig. 4c) first increase with R_H, as one would expect, but reach a maximum for R_H in the range 15–25, after which they start to decrease and level off. These observations indicate that beyond some value of R_H, the plumes generated at the top of the thermochemical piles extract more heat from these piles than at lower heating excess. Piles stop heating up, and less heat is transferred to the core, such that piles are better insulators at moderate than at high excess heating. This behaviour can be understood by noting that the ability of plumes to transfer heat is strongly affected by the ambient heating rate, with larger heating rate decreasing the plume efficiency[42,43]. As piles' heating rate increases, and because the total heating rate is fixed, heating rate in the rest of the mantle decreases. Consequently, plumes can extract more heat from the piles. The larger number of piles at $R_H \geq 30$, leading to broader interface between piles and regular mantle, may further enhance piles' cooling.

https://doi.org/10.1038/s41561-026-02018-w

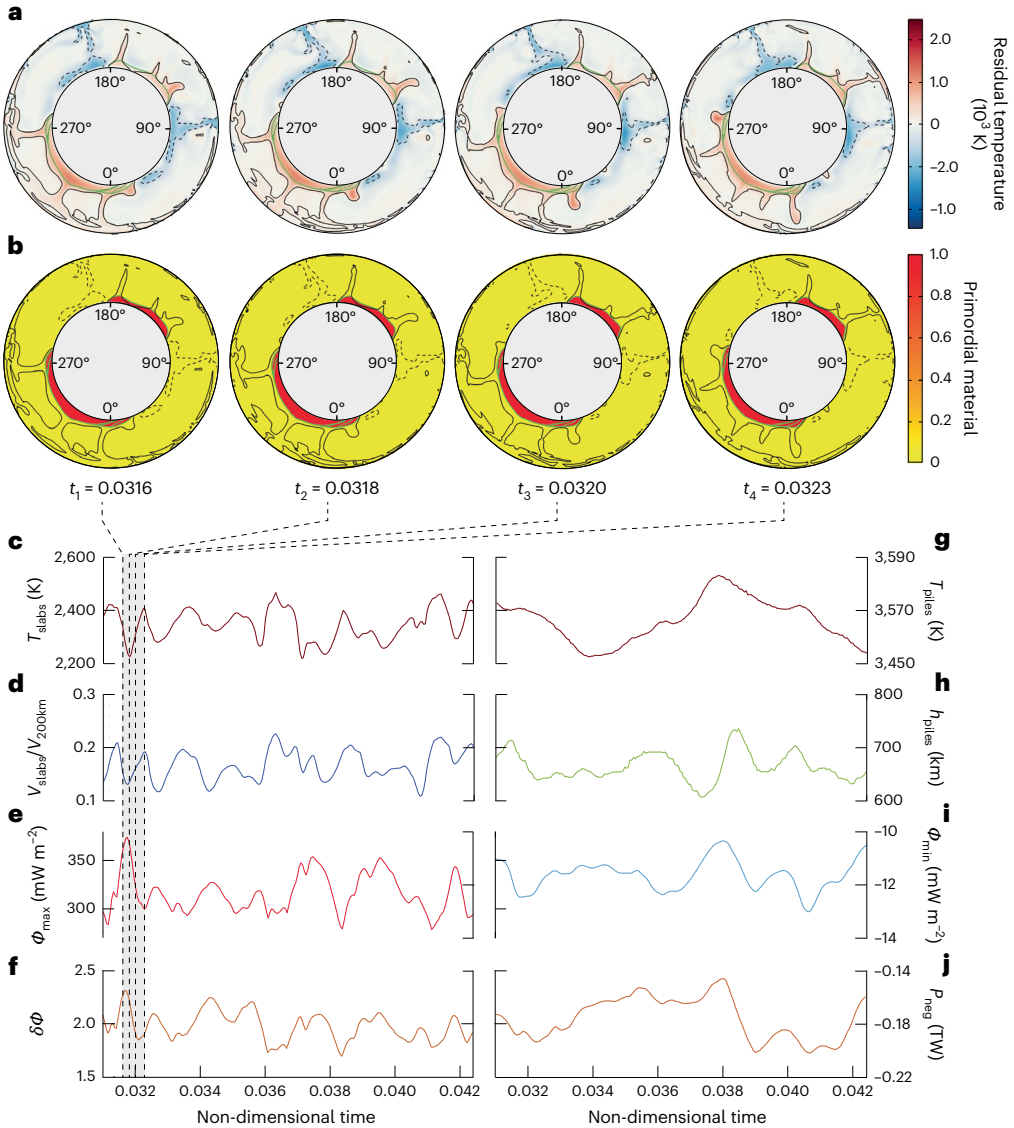

Fig. 3 | Time sequence showing slab arrival and spreading around the CMB. **a**,**b**, Residual temperature (**a**) and composition (**b**), respectively, with lines and contours being similar to those in Fig. 1. **c**–**j**, Plots of the time variations in average slabs temperature in the lowermost 200 km (**c**), slab volume fraction in the lowermost 200 km (**d**), maximum CMB heat flux (**e**), heat flux heterogeneity (**f**), average thermochemical piles temperature (**g**), piles culminating altitude (**h**), minimum CMB heat flux (**i**) and total power in patches of negative CMB heat flux (**j**) (in this latter case, the negative sign is imposed by convention to indicate that heat flows from the mantle to the core). In **c**–**j**, the time axis is graduated in non-dimensional units, the whole duration being equivalent to 4 Gyr. The thermal conductivity temperature exponent is $a = 0.3$, and the piles excess heating ratio is $R_H = 15$.

Time variations of the total power in patches reach an amplitude of ~0.1 TW (Fig. 3j and Extended Data Fig. 5e) and mimic time variations in Φ_{min} (Fig. 3i), with a much lower frequency than the variations in Φ_{max}. This behaviour is related to the presence and evolution of thermochemical piles. In purely thermal models Φ_{min} (which is then associated with plumes roots), vary with a frequency similar to that of Φ_{max}. Also noteworthy, the amount of heat flowing to the core and piles thickness are overall correlated, with thinner piles leading to larger heat flow (Fig. 3h and Extended Data Fig. 6).

Implications for core dynamics and geodynamo

Our findings bring new insights on core dynamics and the geodynamo. For temperature dependence of thermal conductivity and LLSVPs excess heating rate ratio consistent with available constraints, our simulations predict subadiabatic CMB heat flux beneath LLSVPs. Such low heat flux may lead to local stratification at the top of the core[4,5]. Consequent large lateral variations in CMB heat flux leading to regional stratification below LLSVPs superimposed over a mean superadiabatic flux may reconcile seismic studies in favour of stratification at the top of the core[6] and geomagnetic field models with intense flux concentrations[7] that are difficult to reproduce in numerical dynamos with a thick global stratified layer[8].

The amplitude of heat flux heterogeneity, $\delta\Phi$, has long been suspected to exert a strong control on geomagnetic reversals[9,13,44–46]. Combined with low equatorial heat flux (or, equivalently, polar cooling), high $\delta\Phi$ may suppress reversals[13,44,45]. Because LLSVPs are mostly distributed near the equator[20] and, following our findings, associated with subadiatic heat flux, they may trigger local core stratification at low latitudes, and heat flowing to the core at negative patches may amplify this effect. Our simulations further indicate that temporal variations in $\delta\Phi$ are strong, with amplitude in the range of 0.5–1.0, the largest heterogeneity resulting from slabs impacts on the CMB. Combined with subadiabatic conditions in LLSVPs, these variations may play a key role in the occurrence and termination of superchrons[10,11]. In our simulations, timescales

https://doi.org/10.1038/s41561-026-02018-w

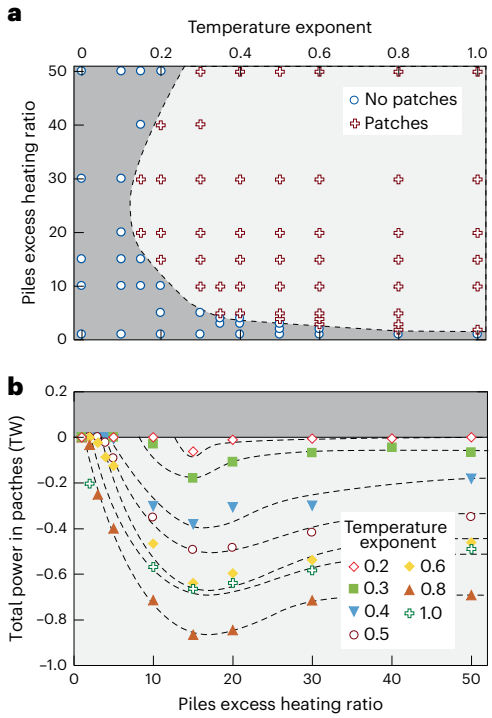

Fig. 4 | Negative heat flux patches occurrence and total power. a, Distribution of simulations featuring patches of negative heat flux (dark-red crosses) as a function of temperature exponent of thermal conductivity (x axis) and piles excess heating ratio (y axis). **b**, Time-averaged (over the last 2 Gyr of simulations) power in patches of negative heat flux as a function of the piles excess heating ratio, R_H, and for different values of the temperature exponent (symbols). The negative sign is imposed by convention to indicate that heat flows from the mantle to the core. The dashed curves are plotted only to show general trends.

for these variations are rather long, ~200 Myr for $\delta\Phi$ and ~1 Gyr for piles oscillations, but may be reduced by prescribing more Earth-like parameter values, for example, a lithosphere rheology favouring slabs descent or a time-dependent internal heating.

Another mechanism possibly controlling geomagnetic reversals is the westward drift of magnetic flux patches induced by westward zonal flow[13,47]. Locally subadiabatic or negative heat flux could, by locally heating up the top of the core, strengthen this westward flow via thermal wind[48] and therefore further suppress reversals occurrence. More generally, long term changes in the locations or altitude of LLSVPs and in the associated locations and intensities of negative patches could partially control the frequency of geomagnetic reversals, either by moving low or negative heat flux regions to higher latitudes or by modulating heat flux beneath LLSVPs. Although in our simulations these changes are limited in amplitude, ~10 mW m^{-2} (Fig. 3g–j and Extended Data Fig. 5), patches of negative heat flux for low a (~0.2–0.3) and/or R_H are weak, such that they may temporarily disappear (Extended Data Fig. 6b). Due to spherical-annulus geometry, spatial variations are also limited but still substantial, with the surfaces of subadiabatic and negative heat flux regions varying by up to 10% of the total CMB area (Extended Data Fig. 5).

Due to their expected high temperature and very low conductivity[37], ULVZs, which are not included in our simulations, could also impact CMB heat flux. Interestingly, these regions might be more mobile than LLSVPs[49]. Three-dimensional spherical simulations of mantle convection are needed to investigate these aspects more in details. Additional geodynamo simulations with boundary conditions accounting for wide equatorial subadiabatic regions and/or local patches of negative heat flux, together with additional experimental data to refine our knowledge of deep mantle minerals thermal conductivities and their temperature dependence, are further needed to precisely determine the consequences of our findings on the magnetic field evolution.

Online content

Any methods, additional references, Nature Portfolio reporting summaries, source data, extended data, supplementary information, acknowledgements, peer review information; details of author contributions and competing interests; and statements of data and code availability are available at https://doi.org/10.1038/s41561-026-02018-w.

References

1. Gubbins, D., Willis, P. W. & Sreenivasan, B. Correlation of Earth's magnetic field with lower mantle thermal and seismic structure. *Phys. Earth Planet. Inter.* **162**, 256–260 (2007).
2. Aubert, J., Amit, H., Hulot, G. & Olson, P. Thermo-chemical flows couple the Earth's inner core growth to mantle heterogeneity. *Nature* **454**, 758–761 (2008).
3. Terra-Nova, F., Amit, H. & Choblet, G. Preferred locations of weak surface field in numerical dynamos with heterogeneous core–mantle boundary heat flux: consequences for the South Atlantic Anomaly. *Geophys. J. Int.* **217**, 1179–1199 (2019).
4. Olson, P. L., Landeau, M. & Reynolds, E. Dynamo tests for stratification below the core–mantle boundary. *Phys. Earth Planet. Inter.* **271**, 1–18 (2017).
5. Mound, J., Davies, C., Rost, S. & Aurnou, J. Regional stratification at the top of the Earth's core due to core–mantle boundary heat flux variations. *Nat. Geosci.* **12**, 575–580 (2019).
6. Kaneshima, S. Array analyses of SmKS waves and the stratification of Earth's outermost core. *Phys. Earth Planet. Inter.* **276**, 234–246 (2018).
7. Amit, H. Can downwelling at the top of the Earth's core be detected in the geomagnetic secular variation? *Phys. Earth Planet. Inter.* **229**, 110–121 (2014).
8. Gastine, T., Aubert, J. & Fournier, A. Dynamo-based limit to the extent of a stable layer atop Earth's core. *Geophys. J. Int.* **222**, 1433–1448 (2020).
9. Olson, P. & Amit, H. Magnetic reversals frequency scaling in dynamos with thermochemical convection. *Phys. Earth Planet. Inter.* **229**, 122–133 (2014).
10. Amit, H. & Olson, P. Lower mantle superplume growth excites geomagnetic reversals. *Earth Planet. Sci. Lett.* **414**, 68–76 (2015).
11. Hounslow, M. W., Domeier, M. & Biggin, A. J. Subduction flux modulates the geomagnetic polarity reversal rate. *Tectonophysics* **742-743**, 34–49 (2018).
12. Yoshimura, Y. The Cretaceous Normal Superchron: a mini-review of its discovery, short reversal events, paleointensity, paleosecular variations, paleoenvironment, volcanism, and mechanism. *Front. Earth Sci.* **10**, 834024 (2022).
13. Frasson, T., Schaeffer, N., Nataf, H.-C. & Labrosse, S. Geomagnetic dipole stability and zonal flows controlled by mantle heat flux heterogeneities. *Geophys. J. Int.* **240**, 1481–1504 (2025).
14. van der Hilst, R. D., Widiyantoro, S. & Engdahl, E. R. Evidence for deep mantle circulation from seismic tomography. *Nature* **386**, 578–584 (1997).
15. Fukao, Y., Widiyantoro, S. & Obayashi, M. Stagnant slabs in the upper and lower transition regions. *Rev. Geophys.* **39**, 291–323 (2001).
16. Wookey, J., Stackhouse, S., Kendall, J. M., Brodholt, J. & Price, G. D. Efficacy of the post-perovskite phase as an explanation for lowermost-mantle seismic properties. *Nature* **438**, 1004–1007 (2005).
17. Hirose, K. in *Post-perovskite the Last Mantle Phase Transition*, *Geophysical Monograph* Vol. 174 (eds Hirose, K. et al.) 19–35 (American Geophysical Union, 2007).

18. Yu, S. & Garnero, E. J. Ultralow velocity zones: a global assessment. *Geochem. Geophys. Geosyst.* **19**, 396–414 (2018).
19. Garnero, E. J., McNamara, A. & Shim, S.-H. Continent-sized anomalous zones with low seismic velocity at the base of Earth's mantle. *Nat. Geosci.* **9**, 481–489 (2016).
20. Richards, F. D., Hoggard, M. J., Ghelichkhan, S., Koelemeijer, P. & Lau, H. C. P. Geodynamic, geodetic, and seismic constraints favour deflated and dense-cored LLVPs. *Earth Planet. Sci. Lett.* **602**, 117964 (2023).
21. Koelemeijer, P. in *Mantle Convection and Surface Expressions* (eds Marquardt, J. et al.) Ch. 9 (American Geophysical Union, 2021).
22. Trampert, J., Deschamps, F., Resovsky, J. & Yuen, D. A. Probabilistic tomography maps significant chemical heterogeneities in the lower mantle. *Science* **306**, 853–856 (2004).
23. Deschamps, F., Cobden, L. & Tackley, P. J. The primitive nature of large low shear-wave velocity provinces. *Earth Planet. Sci. Lett.* **349-350**, 198–208 (2012).
24. Klemens, P. G., White, G. K. & Tainsh, R. J. Scattering of lattice waves by point defects. *Philos. Mag.* **7**, 1323–1335 (1962).
25. Dalton, D. A., Hsieh, W.-P., Hohensee, G. T., Cahill, D. G. & Goncharov, A. F. Effect of mass disorder on the lattice thermal conductivity of MgO periclase under pressure. *Sci. Rep.* **3**, 2400 (2013).
26. Yuan, Q. et al. Moon-forming impactor as a source of Earth's basal mantle anomalies. *Nature* **623**, 95–99 (2023).
27. Labrosse, S., Hernlund, J. W. & Coltice, N. A crystallizing dense magma ocean et the base of the Earth's mantle. *Nature* **450**, 866–869 (2007).
28. Kellogg, L. H., Hager, B. H. & ven der Hilst, R. D. Compositional stratification in the deep mantle. *Science* **283**, 1881–1884 (1999).
29. Tackley, P. J. Modelling compressible mantle convection with large viscosity contrasts in three-dimensional spherical shell using the yin-yang grid. *Phys. Earth Planet. Inter.* **171**, 7–18 (2008).
30. Guerrero, J. M. et al. The combined effect of heterogeneous thermal conductivity, chemical density contrast and heat-producing elements enrichment on the stability of primordial reservoirs above the core–mantle boundary. *Earth Planet. Sci. Lett.* **637**, 118688 (2024).
31. Hernlund, J. & Tackley, P. J. Modeling mantle convection in the spherical annulus. *Phys. Earth Planet. Inter.* **171**, 48–54 (2008).
32. Hsieh, W.-P., Deschamps, F., Okuchi, T. & Lin, J. F. Reduced lattice thermal conductivity of Fe-bearing bridgmanite in Earth's deep mantle. *J. Geophys. Res. Solid Earth* **122**, 4900–4917 (2017).
33. Hsieh, W.-P., Deschamps, F., Okuchi, T. & Lin, J. F. Effects of iron on the lattice thermal conductivity of Earth's deep mantle and implications for mantle dynamics. *Proc. Natl Acad. Sci. USA* **115**, 4099–4104 (2018).
34. Chang, Y. Y., Hsieh, W. P., Tan, E. & Chen, J. Hydration-reduced lattice thermal conductivity of olivine in Earth's upper mantle. *Proc. Natl Acad. Sci. USA* **114**, 4078–4081 (2017).
35. Manthilake, G. M., de Koker, N., Frost, D. J. & McCammon, C. A. Lattice thermal conductivity of lower mantle minerals and heat flux from Earth's core. *Proc. Natl Acad. Sci. USA* **108**, 17901–17904 (2011).
36. Zhang, Y., Yoshino, T. & Osako, M. Effect of iron content on thermal conductivity of ferropericlase: implications for planetary mantle dynamics. *Geophys. Res. Lett.* **50**, e2022GL101769 (2023).
37. Hsieh, W.-P. et al. Spin transition in magnesiowüstite: ultralow thermal conduction in ultralow velocity zones. *Nat. Commun.* **16**, 10431 (2025).
38. Jaupart, C., Labrosse, S., Lucazeau, F. & Mareschal, J.-C. in *Treatise on Geophysics* 2nd edn, Vol. 7 (ed. Schubert, G.) 218–251 (Elsevier, 2015).
39. Cottaar, S. & Lekic, V. Morphology of seismically slow lower-mantle structures. *Geophys. J. Int.* **207**, 1122–1136 (2016).
40. Zhang, N. & Zhong, S. Heat fluxes at the Earth's surface and core–mantle boundary since Pangea formation and their implications for geomagnetic superchrons. *Earth Planet. Sci. Lett.* **306**, 205–216 (2010).
41. Hsieh, W.-P. et al. Moderate thermal conductivity of Fe–Ni–Si alloy at Earth's core conditions: implications for core thermal evolution and geodynamo. *Geophys. Res. Lett.* **52**, e2025GL117576 (2025).
42. Sotin, C. & Labrosse, S. Three-dimensional thermal convection in an iso-viscous, infinite Prandtl number fluid heated from within and from below: application to the transfer of heat through planetary mantles. *Phys. Earth Planet. Inter.* **112**, 171–190 (1999).
43. Deschamps, F., Tackley, P. J. & Nakagawa, T. Temperature and heat flux scalings for isoviscous thermal convection in spherical geometry. *Geophys. J. Int.* **182**, 137–154 (2010).
44. Olson, P., Coe, R. S., Driscoll, P. E., Glatzmaier, G. A. & Roberts, P. A. Geodynamo reversal frequency and heterogeneous core–mantle boundary heat flow. *Phys. Earth Planet. Inter.* **180**, 66–79 (2010).
45. Terra-Nova, F. & Amit, H. Regionally-triggered geomagnetic reversals. *Sci. Rep.* **14**, 9639 (2024).
46. Glatzmaier, G., Coe, R., Hongre, L. & Roberts, P. The role of the earth's mantle in controlling the frequency of geomagnetic reversals. *Nature* **401**, 885–890 (1999).
47. Jones, C. A. & Tsang, Y.-K. Low inertia reversing geodynamos. *Phys. Earth Planet. Inter.* **360**, 107303 (2025).
48. Pedlosky, J. *Geophysical Fluid Dynamics* (Springer, 1987).
49. Li, M., McNamara, A. K., Garnero, E. J. & Yu, S. Compositionally-distinct ultra-low velocity zones on Earth's core–mantle boundary. *Nat. Commun.* **8**, 177 (2017).

Methods

Numerical set-up

We perform numerical simulations of thermochemical convection with StagYY[29], solving conservation of mass, energy, momentum and composition for a compressible, infinite Prandtl number fluid. The numerical set-up is very close to that used in ref. 30, with some differences, mainly the grid resolution. All simulations are run in non-dimensional units and rescaled during postprocessing. Supplementary Table 1 lists the input parameters values.

Geometry and general physical properties. Conservation equations are solved on a spherical annulus[31] sampled by 256 vertical and 2,048 longitudinal nodes. In addition, we prescribed grid refinement at the top and at the bottom of the annulus to describe more precisely the thermal boundary layers in these regions. The ratio between the radius of the core and the total radius is set to its Earth value, that is, $f = 0.55$. The bottom and surface boundaries are free slip and isothermal, with surface and bottom temperature fixed to 300 K and 3,750 K, respectively.

A phase transition is added at a depth of 660 km, modelling the transformation of ringwoodite into bridgmanite and ferro-periclase at 660 km. For this, we define a point on the phase boundary and a Clapeyron slope, Γ_{660}. Here, we imposed $d = 660$ km and $T = 1{,}900$ K as anchor point, and $\Gamma_{660} = -2.5$ MPa K^{-1}. We did not include the phase transition to pPv.

Viscosity η_b is allowed to vary with depth, temperature and composition. An additional viscosity ratio $\Delta\eta_{660} = 30$ is added at the 660-km phase transition. Furthermore, to avoid the formation of stagnant lid at the top of the system, we impose a yield stress. The effective viscosity η is then fully described by

$$\eta = \frac{1}{\frac{1}{\eta_b} + \frac{1}{\eta_Y}}, \tag{A1}$$

where

$$\eta_Y = \frac{\sigma_0 + \dot{\sigma}_z P}{2\dot{\epsilon}} \tag{A2}$$

is the yield viscosity, and

$$\eta_b(d, T, C_{prim}) = \eta_0 \left[1 + 29H(d - 660)\right] \exp\left[V_a \frac{d}{D} + E_a \frac{\Delta T_S}{(T + T_{off})} + K_a C_{prim}\right] \tag{A3}$$

The yield viscosity (equation (A2)) is defined from the yield stress, $\sigma_Y = \sigma_0 + \dot{\sigma}_P P$, and the second invariant of the stress tensor, $\dot{\epsilon}$. The yield stress is set to σ_0 at the surface, here equivalent to 290 MPa, and increases with pressure following a gradient (with respect to pressure) of $\dot{\sigma}_P$, here equal to 0.01. In equation (A3), η_0 is a reference viscosity, H the Heaviside step function, d the depth, D the mantle thickness, C_{prim} the concentration in dense material (see below), ΔT_S the superadiabatic temperature difference across the system and T_{off} a temperature offset, which is added to the temperature to reduce the viscosity jump across the top thermal boundary layer and which we fixed to $T_{off} = 0.88\Delta T_S$. The reference viscosity η_0 is defined for the surface value of the reference adiabat (that is, $T_{as} = 0.64\Delta T_S$) and at regular composition ($C_{prim} = 0$). The viscosity variations with temperature are controlled by E_a, modelling the activation energy. To quantify the thermally induced increase of viscosity, we define a potential thermal viscosity ratio as $\Delta\eta_T = \exp(E_a)$. However, due to the adiabatic increase of temperature and to the temperature offset, the effective top-to-bottom thermal viscosity contrast is smaller than $\Delta\eta_T$ by about two orders of magnitude. Here, we fixed E_a to 16.118, corresponding to $\Delta\eta_T = 10^7$, and equivalent to an activation energy of ~335 kJ mol^{-1}. The viscosity variations with depth are controlled by V_a, modelling the activation volume, and which we fixed to 2.303. Combined with the viscosity jump at 660 km but excluding the decrease due to adiabatic increase of temperature and the thermally induced increase in thermal boundary layers, this leads to a total top-to-bottom increase in viscosity by a factor 300. The viscosity variations with composition are controlled by the parameter K_a, and the viscosity ratio between primordial and regular material (or chemical viscosity ratio) is given by $\Delta\eta_C = \exp(K_a)$. In this study, we impose primordial material to be more viscous than regular material with $\Delta\eta_C = 30$, accounting for the fact that if dense material is enriched in bridgmanite[22,50], it may be more viscous than surrounding mantle[51].

Because the fluid properties (density, viscosity, thermal diffusivity and thermal expansion) are allowed to vary throughout the system, the definition of the Rayleigh number is non-unique. In our simulations, we prescribed a reference Rayleigh number Ra_0, defined at surface values of the thermodynamic parameters and reference viscosity η_0. Here, we set Ra_0 to 3.0×10^8, leading to an effective Rayleigh number (that is, the Rayleigh number at the volume average viscosity) from about 10^6 to 2.0×10^6, depending on the case. In particular, because cases we higher excess heating in piles of dense material are colder, they are slightly more viscous and have a lower Rayleigh number than other cases.

Thermochemical field. Our simulations include two types of material, modelling the regular mantle and a chemically distinct (or primordial) material, respectively. The latter accounts for chemical heterogeneities that may be present at the bottom of the mantle as a result of early differentiation, resulting in the LLSVPs observed by seismic tomography maps. The compositional field is modelled with a collection of about 21 million tracers, equivalent to an average number of tracers per cell of 40, which is enough to properly model entrainment[52]. Tracers are of two types, modelling the regular mantle and primordial material, respectively, and are advected following a fourth-order Runge–Kutta method. At each time step, the compositional field is inferred from the concentration C_{prim} of particles of primordial material in each cell and varies between 0 for a cell filled with regular material only and 1 for a cell filled with primordial material only. The primordial material is initially distributed in a basal layer. The thickness of this layer is controlled by the volume fraction of dense material, X_{prim}, which we fixed to 4%. The primordial material is assumed to be denser than the regular (pyrolitic) mantle, and the density contrast between the two materials is controlled by the buoyancy ratio, here defined with respect to a reference density that increases with depth following a thermodynamical model of Earth's mantle

$$B = \frac{\Delta\rho_c(d)}{\alpha_S \rho(d) \Delta T_S}, \tag{A4}$$

where $\Delta\rho_c(d)$ is the density contrast between dense and regular material, α_S the surface thermal expansion, $\rho(d)$ the reference density at depth z and ΔT_S is the superadiabatic temperature jump. The buoyancy ratio is fixed to $B = 0.23$, which, taking $\alpha_S = 5.0 \times 10^{-5}$ K^{-1}, $\rho_{bot} = 4{,}950$ kg m^{-3} and $\Delta T_S = 2{,}500$ K, leads to a density contrast between dense and regular material, $\Delta\rho_C$, of 142 kg m^{-3} at the bottom of the system. For comparison, we also run a simulation with $B = 0.15$, leading to $\Delta\rho_C = 93$ kg m^{-3}.

Heat sources. The system is heated both from the bottom and from within. Compressibility generates additional sinks and sources of heat that are controlled by the dissipation number, Di, which varies with depth. We fixed the surface value of this number to $Di_S = 1.2$. The rates of internal heating in the regular mantle and in the primordial material are different, with primordial material assumed to have excess heating, controlled with the excess heating ratio, R_H. This difference accounts for the fact that if primordial is related to the last stages of the crystallization of magma ocean[27], it may have been enriched in HPE.

Estimates of excess heating ratio based on the volume of LLSVPs[39,53] may range between 10 and 100, depending on the assumed mantle in HPE[54,55]. Piles of dense material were further shown to remain stable even for strong enrichment (up to excess heating ratio of 100)[53]. The input internal heating rate, H, is then given by

$$H = \frac{H_{\mathrm{tot}}}{\left[1 + X_{\mathrm{prim}}\left(R_{\mathrm{H}} - 1\right)\right]} \tag{A5}$$

and is chosen such that the total heating rate, H_{tot}, is equal to 11 TW, which is the median estimate of the heat generated in the mantle[38] and correspond to a surface heat flux of 21.6 mW m^{-2}. Here, we performed simulations for values of R_{H} in the range 1 (no excess heating in primordial material) to 50. To explore the upper excess heating bound for the formation of patches of negative heat flux, we further run two additional cases with $R_{\mathrm{H}} = 100$. Note that because H_{tot} is fixed to the same value for all simulations, an increase in the excess heating ratio in piles of primordial material implies a decrease of the rate of heating in the regular mantle (Supplementary Fig. 1).

Thermal conductivity. A key aspect of our simulations is that they account for variations of thermal conductivity with depth (pressure), temperature and composition. Supplementary Fig. 2 illustrates these variations for initial profiles of temperature and composition.

Thermal conductivity of mantle mineral increase with pressure. Here, we modelled the depth-dependence with a parameterization based on experimental data for olivine[34], bridgmanite[32] and ferro-periclase[33]. In the lower mantle, this parameterization is defined assuming a mix of 80% iron–aluminium bridgmanite and 20% ferro-periclase along an adiabat of 300 K. Depth-dependence for each end-member is following the pressure-dependent parameterizations built in ref. 56 and by translating pressure to depth following PREM[57]. Conductivity is then obtained from geometric average of Hashin–Shtrikman upper and lower bounds[58] of individual conductivities. In the lower mantle, the non-dimensional conductivity is then given as a function of the non-dimensional depth by

$$\tilde{k}_d = 5.33\left(1 + 4.98\tilde{d} - 0.81\tilde{d}^2\right)/k_{\mathrm{S}}, \tag{A6}$$

where k_{S} is the surface conductivity, which we here fix to 3.0 W m^{-1} K^{-1}. For the upper mantle, we build a polynomial assuming that the surface conductivity is equal, again, to 3.0 W m^{-1} K^{-1}, and that the conductivity and its derivative at a depth of 660-km depth (corresponding to a non-dimensional depth of 0.228) are continuous with those defined for the lower mantle (equation (A6)). The resulting polynomial is given by

$$\tilde{k}_d = 3.0\left(1 + 15.66\tilde{d} - 16.38\tilde{d}^2\right)/k_{\mathrm{S}}. \tag{A7}$$

With these parameterizations, the intrinsic (that is, excluding thermal and compositional effects) bottom to top ratio in thermal conductivity is therefore about 9.

Temperature dependence is assumed to follow a $1/T^a$ law. The reference temperature is taken at the surface, such that the non-dimensional conductivity variations with temperature is given by

$$\tilde{k}_T = \left(\frac{T_{\mathrm{surf}}}{\Delta T \tilde{T}}\right)^a, \tag{A8}$$

where T_{surf} is the surface temperature, fixed to 300 K, ΔT_{S} the superadiabatic jump, fixed to 2,500 K and $\tilde{T}$ the local non-dimensional temperature. The value of the exponent a may be different for different minerals or aggregates of minerals. For iron-bearing material, available mineral physics data[24,25,35–37], while incomplete, point to values in the range 0.2–0.5. Here, we tested values of a from 0 to 1. Although they may not be realistic for mantle materials, values of a lower than 0.2 or larger than 0.5 help to understand the impact of temperature-dependent thermal conductivity on the evolution of the system and on the heat flux at the CMB.

Compositional dependence is assumed to be linear between two end-member compositions

$$\tilde{k}_C = 1 + \left(R_{\mathrm{C}} - 1\right) C_{\mathrm{prim}}, \tag{A9}$$

where R_{C} is the ratio between conductivities of enriched and regular material, and C_{prim} is the local fraction of dense material. The conductivity compositional dependence is set to 1 for regular material ($C_{\mathrm{prim}} = 0$). For instance, a decrease by 20%, which may correspond to dense material enrichments of in iron by 3.0% and in bridgmanite by 10%[32], implies $R_{\mathrm{C}} = 0.8$. Here, we fixed the value of R_{C} to 0.8 in all simulations.

Finally, the non-dimensional conductivity corrected for thermal, pressure and compositional effects is given by $\tilde{k} = \tilde{k}_d \times \tilde{k}_T \times \tilde{k}_C$ and rescaled with the surface conductivity k_{S}, which, again, we fixed to 3.0 W m^{-1} K^{-1}.

Simulations, postprocessing and derived quantities

We performed more than 80 simulations using the set-up described in the previous section. All simulations start with a transient phase during which the system is heating up. After, this phase, the flow organizes following a set of downwellings (slabs) and upwellings (plumes), and the heat transfer reach a quasi-stationary state, meaning that the top and bottom heat flux oscillates in time around nearly constant values (Supplementary Fig. 3). Supplementary Tables 2 and 3 list selected output parameters (including temperature, composition and CMB heat flux statistics) averaged out in the non-dimensional time window 0.0367–0.0424, corresponding to a duration of 2 Gyr.

Temperature, thermal conductivity and other properties are rescaled during the postprocessing using the characteristic values indicated in Supplementary Table 1. Adiabatic effects on temperature are taken into account when solving the energy and momentum conservation equations, but for practical reasons, output temperature fields do not include these effects. When rescaling temperature, we and therefore corrected it for the adiabatic increase of temperature with pressure. The dimensional 'real' temperature at a given altitude z and longitude φ, $T(z, \varphi)$, is then obtained from the non-dimensional, uncompressed temperature, $\tilde{T}(z, \varphi)$, following

$$T(z, \varphi) = \left[\tilde{T}(z, \varphi) + \tilde{T}_{\mathrm{top}}\right] a_{\mathrm{c}}(z)\, \Delta T_{\mathrm{S}} \tag{A10}$$

where $\tilde{T}_{\mathrm{top}}$ is the surface non-dimensional temperature, here fixed to 0.12 (equivalent to a dimensional temperature of $T_{\mathrm{surf}} = 300$ K), $\Delta T_{\mathrm{S}} = 2{,}500$ K is the superadiabatic temperature jump, and $a_{\mathrm{c}}(z)$ the adiabatic correction at altitude z given by

$$a_{\mathrm{c}}(z) = \exp\left[\int_0^d \mathrm{Di}_{\mathrm{S}} \frac{\alpha(z)}{C_{\mathrm{P}}(z)} \mathrm{d}r\right], \tag{A11}$$

where Di_{S} is the surface dissipation number, r the elevation above the CMB, d the depth and $\alpha(z)$ and $C_{\mathrm{P}}(z)$ are the thermal expansion and heat capacity as a function of altitude. These two functions are defined as part of a reference thermodynamical model involved in the compressible form of conservation equations[59]. Practically, α decreases by a factor 5 from the surface to the CMB, whereas C_{P} is constant with depth. The adiabatic correction defined in equation (A10) then varies from 1.0 at the surface to about 1.55 at the CMB. For the expected temperature dependence of mantle minerals ($0.25 \le a \le 0.5$), piles are hotter than the regular mantle by 300–500 K and may locally reach temperatures of 4,000 K and slightly higher. At such temperatures, and following recent melting curves of mantle material[60], piles may locally be partially molten, a situation that is not accounted for in our simulations. Note that partial melting, if present, may explain the ULVZs observed within LLSVPs[18]. For stronger temperature dependences, melting may be more

widespread, but one should keep in mind that such high values of a are unrealistic for mantle material.

We calculate the local CMB heat flux from the temperature distributions of our simulations using the temperature on two lowermost grid points, T_1 and T_2, plus the CMB temperature, T_{CMB}, here fixed to 3,750 K. More precisely, we first estimate the temperature gradient by writing T_1 and T_2 as Taylor expansions of altitude z to the second order and by combining these equations to cancel the second derivative of temperature. The heat flux at longitude is then given by

$$\Phi_{CMB}(\varphi) = k_{CMB}\frac{(r_z^2-1)\,T_{CMB} + T_1(\varphi) - r_z^2 T_2(\varphi)}{z_1\,(1-r_z)}, \tag{A12}$$

where z_1 and z_2 are the altitudes of the two lowermost grid points, and $r_z = z_1/z_2$. As T_{CMB} is fixed, the thermal conductivity on the CMB, k_{CMB}, is also constant throughout the CMB, but its value decreases with increasing temperature dependence (increasing exponent a, see previous section). Using this scheme allows, in particular, to better capture the curvature of the temperature profile in the thermal boundary layer. While our calculations are performed in a spherical annulus, we rescale the CMB power with the surface of the Earth core. In particular, the total power in the patches of negative heat flux, P_{neg}, is deduced by integrating the heat flux over the whole surface fraction S_{neg}, where this flux in negative, and multiplied by the core surface. Alternatively, and more straightforwardly, one may simply calculate P_{neg} from the negative patches average heat flux, $<\Phi_{neg}>$, following

$$P_{neg} = 4\pi r_{CMB}^2 P_{neg}\left\langle \Phi_{neg}\right\rangle. \tag{A13}$$

We further defined the lateral CMB heat heterogeneity with the ratio

$$\delta\Phi = \frac{(\Phi_{max}-\Phi_{min})}{2\left\langle \Phi_{CMB}\right\rangle}, \tag{A14}$$

where Φ_{max}, Φ_{min} and $<\Phi_{CMB}>$ are the maximum, minimum and average heat flux, respectively. This definition is similar to that q^*, which is often used to measure heterogeneity of the CMB heat flux imposed in simulations of core dynamics, except that we set the core adiabatic heat flux, Φ_{adia}^{core}, to zero. Here, we preferred to use $\delta\Phi$ first because it gives a more direct measure of CMB heat flux heterogeneity on the mantle side and, second, because in our simulations the values of $<\Phi_{CMB}>$, which are close to or within the current estimated range of 25–110 mW m^{-2} (ref. 38), are also close to the estimates of Φ_{adia}^{core}, leading to very high (and in some case negative) q^*. It should also be noted that a high Φ_{adia}^{core} (~100 mW m^{-2} or more, corresponding to a power of 15 TW) would prevent the core to cool down and the geodynamo to operate.

Calculations of mean specific properties (for example, thermal conductivity or temperature) within slabs and plumes or of the altitude of piles of dense material requires to define the boundaries of these regions. Piles of dense material have very sharp boundary, meaning that the fraction of dense material at a given location, C_{prim}, decreases nearly instantaneously from 1 to 0 as the border is crossed. Here, we define the piles border with the isosurface $C_{prim} = 0.9$. For the reason we just mentioned, choosing smaller values does substantially modify our results. To define the boundaries of plumes and slabs, we use a classical method based on the difference between the minimum, maximum and mean values of the temperature at a given depth[61]. Plumes and slabs are then defined as region with temperature larger (respectively, smaller) than

$$T_{plume}(z) = T_m(z) + c_{plume}\left[T_{max}(z) - T_m(z)\right] \tag{A15}$$

and

$$T_{slab}(z) = T_m(z) - c_{slab}\left[T_m(z) - T_{min}(z)\right], \tag{A16}$$

with c_{plume} and c_{slab} being two constants, which we here fixed to 0.5 and 0.6, respectively.

Data availability

The numerical modelling data generated in this study are available via Zenodo at https://doi.org/10.5281/zenodo.19181104 (ref. 62).

Code availability

The numerical code StagYY is the property of Paul J. Tackley and Eidgenössische Technische Hochschule Zürich. Researchers interested in using StagYY should contact Paul J. Tackley (paul.tackley@erdw.ethz.ch). The codes processing StagYY outputs used for this study are available on request to F.D. (frederic@earth.sinica.edu.tw).

References

50. Mosca, I., Cobden, L., Deuss, A., Ritsema, J. & Trampert, J. Seismic and mineralogical structures of the lower mantle from probabilistic tomography. *J. Geophys. Res.* **117**, B06304 (2012).
51. Yamazaki, D. & Karato, S.-I. Some mineral physics constraints on the rheology and geothermal structure of Earth's lower mantle. *Amer. Mineral.* **86**, 385–391 (2001).
52. Tackley, P. J. & King, S. D. Testing the tracer ratio method for modeling active compositional fields in mantle convection simulations. *Geochem. Geophys. Geosyst.* **4**, 8302 (2003).
53. Citron, R. I. et al. Effects of heat-producing elements on the stability of deep mantle thermochemical piles. *Geochem. Geophys. Geosyst.* **21**, e2019GC008895 (2020).
54. Arevalo, R. & McDonough, W. F. Chemical variations and regional diversity observed in MORB. *Chem. Geol.* **271**, 70–85 (2010).
55. Workman, R. K. & Hart, S. R. Major and trace element composition of the depleted MORB mantle (DMM). *Earth Planet. Sci. Lett.* **231**, 53–72 (2005).
56. Deschamps, F. & Hsieh, W.-P. Lowermost mantle thermal conductivity constrained from experimental data and tomographic models. *Geophys. J. Int.* **219**, S115–S136 (2019).
57. Dziewonski, A. M. & Anderson, D. L. Preliminary reference earth model. *Phys. Earth Planet. Inter.* **25**, 297–356 (1981).
58. Hashin, Z. & Shtrikman, S. A variational approach to the theory of the effective magnetic permeability of multiphase materials. *J. Appl. Phys.* **33**, 3125–3131 (1962).
59. Tackley, P. J. in *The Core–Mantle Boundary Region, Geodynamics Series* Vol. 28 (eds Gurnis, M. et al.) 231–253 (American Geophysical Union, 1998).
60. Pierru, R. et al. Solidus melting of pyrolite and bridgmanite: implication for the thermochemical state of the Earth's interior. *Earth Planet. Sci. Lett.* **595**, 11770 (2022).
61. Labrosse, S. Hotspots, mantle plumes and core heat loss. *Earth Planet. Sci. Lett.* **199**, 147–156 (2002).
62. Deschamps, F., Guerrero, J. M., Amit, H., Terra-Nova, F. & Hsieh, W.-P. Negative core–mantle boundary heat flux beneath low shear-wave velocity provinces. *Zenodo* https://doi.org/10.5281/zenodo.19181104 (2026).

Acknowledgements

The research reported in this article was funded by Academia Sinica grant no. AS-IA-113-M02 to F.D. and National Science and Technology Council (NSTC) of Taiwan grant nos. 113-2116-M-001-021 to J.M.G. and 114-2628-M-001-004 to W.-P.H. H.A. and F.T.-N. further benefited of financial support from the French Agence Nationale de Recherche, project no. DYRE-COMB (grant no. ANR-22-CE49-0016–01).

Author contributions

F.D. conceived the project, performed and analysed numerical simulations of mantle convection, and contributed to analysis tools. J.M.G. analysed numerical simulations of mantle convection and contributed to analysis tools. H.A. and F.T.-N. provided expertise on core dynamics and geodynamo. W.-P.H. provided expertise on mantle thermal conductivity and their measurements. All authors wrote the article.

Competing interests
The authors declare no competing interests.

Additional information
Extended data is available for this paper at https://doi.org/10.1038/s41561-026-02018-w.

Supplementary information The online version contains supplementary material available at https://doi.org/10.1038/s41561-026-02018-w.

Correspondence and requests for materials should be addressed to Frédéric Deschamps.

Peer review information *Nature Geoscience* thanks the anonymous reviewer(s) for their contribution to the peer review of this work. Peer reviewer reports are available. Primary Handling Editor: Alison Hunt, in collaboration with the *Nature Geoscience* team.

https://doi.org/10.1038/s41561-026-02018-w

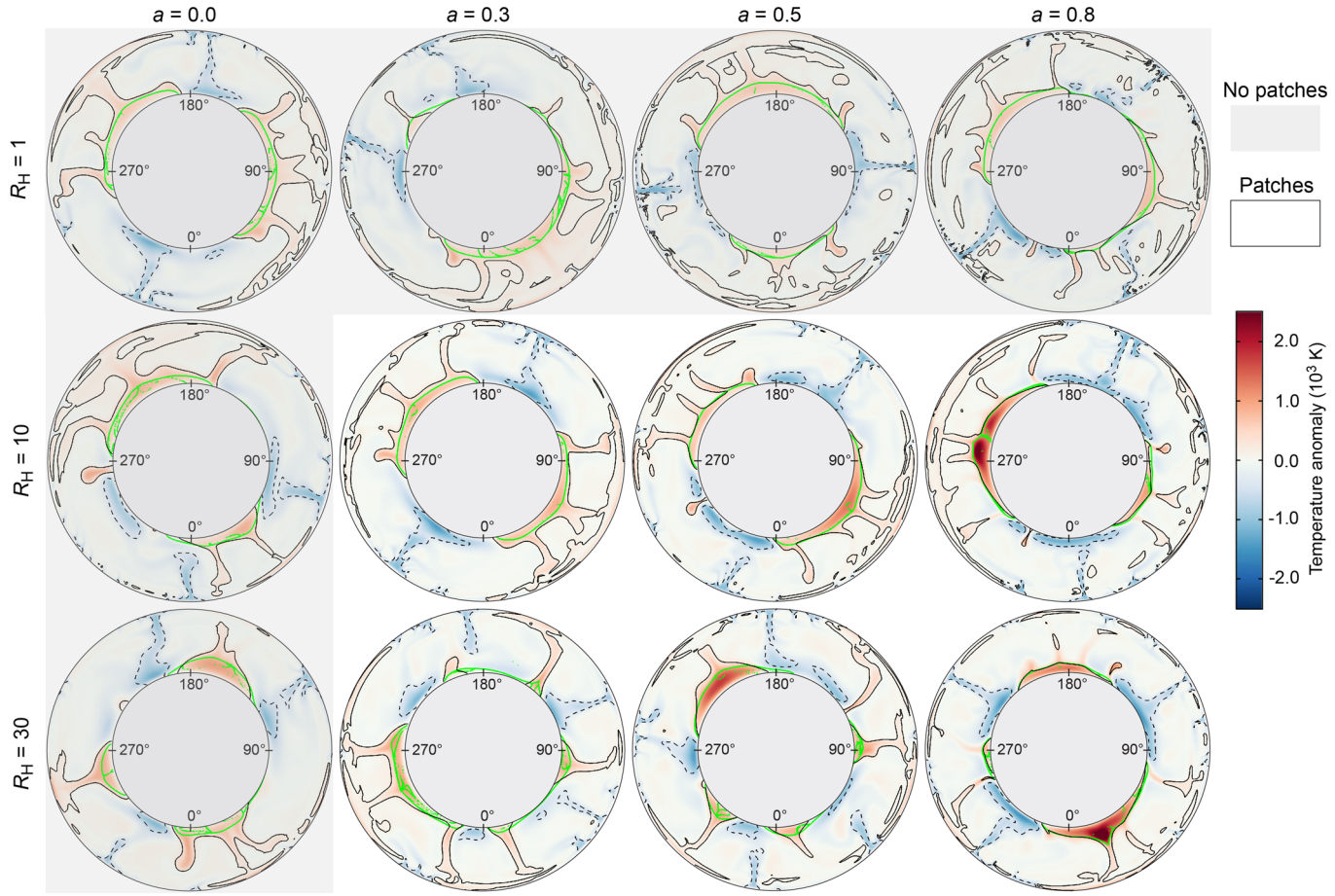

Extended Data Fig. 1 | Snapshots of the residual temperature for selected simulations. Different combinations of the thermal conductivity temperature exponent, a, and of the excess heating ratio in piles of dense material, R_H, are considered. The plain and dashed black contours represent the boundaries of the plumes and downwellings (as defined in the Methods), respectively, and the green contours show the roof of the piles. The gray shaded bands indicate the cases for which we observe patches of negative heat flux at the CMB. Snapshots are taken at the end of each simulation.

https://doi.org/10.1038/s41561-026-02018-w

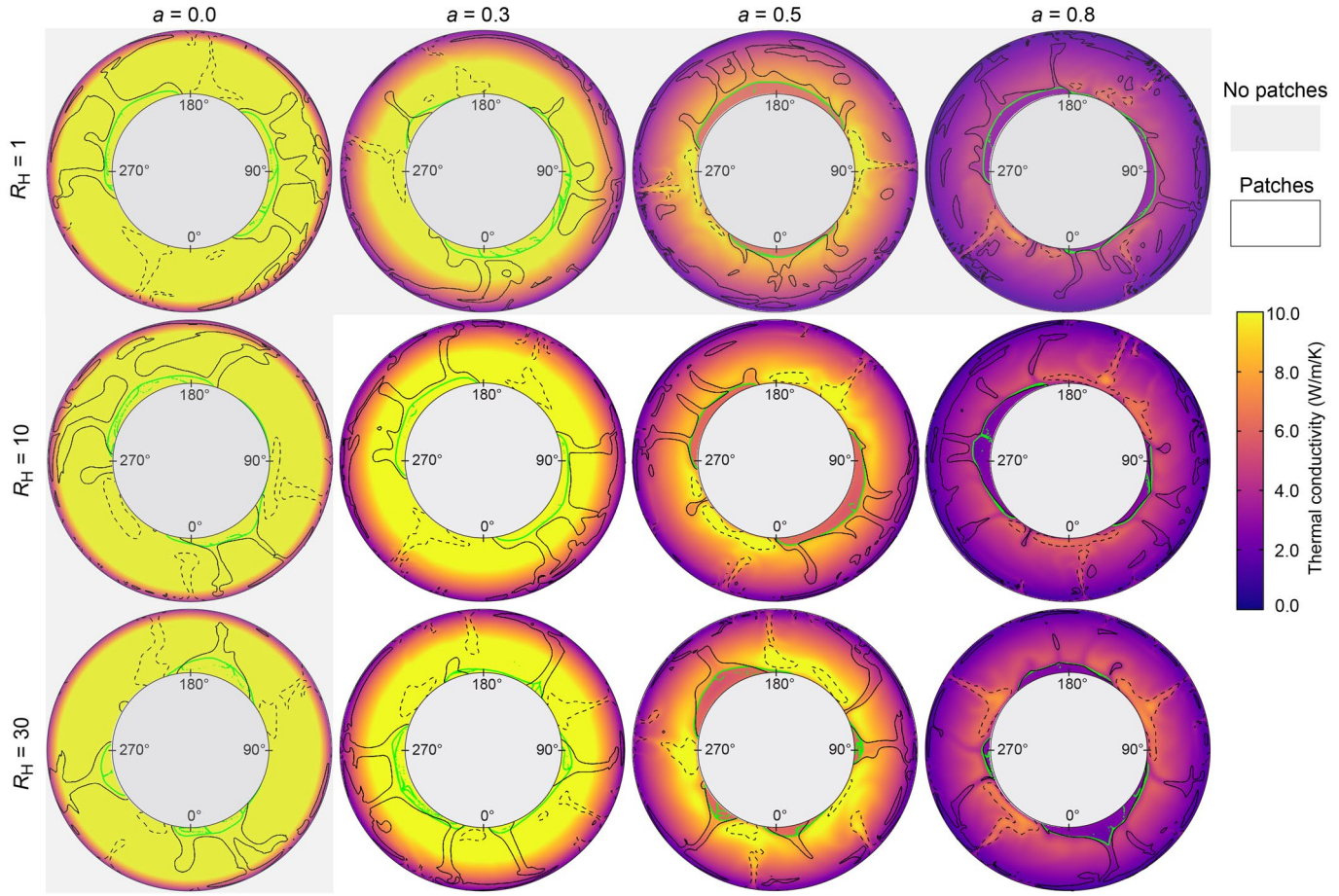

Extended Data Fig. 2 | Snapshots of the thermal conductivity for selected simulations. Different combinations of the thermal conductivity temperature exponent, a, and of the excess heating ratio in piles of dense material, R_H, are considered. The plain and dashed black contours represent the boundaries of the plumes and downwellings (as defined in Methods), respectively, and the green contours show the roof of the piles. The gray shaded bands indicate the cases for which we observe patches of negative heat flux at the CMB. Snapshots are taken at the end of each simulation.

https://doi.org/10.1038/s41561-026-02018-w

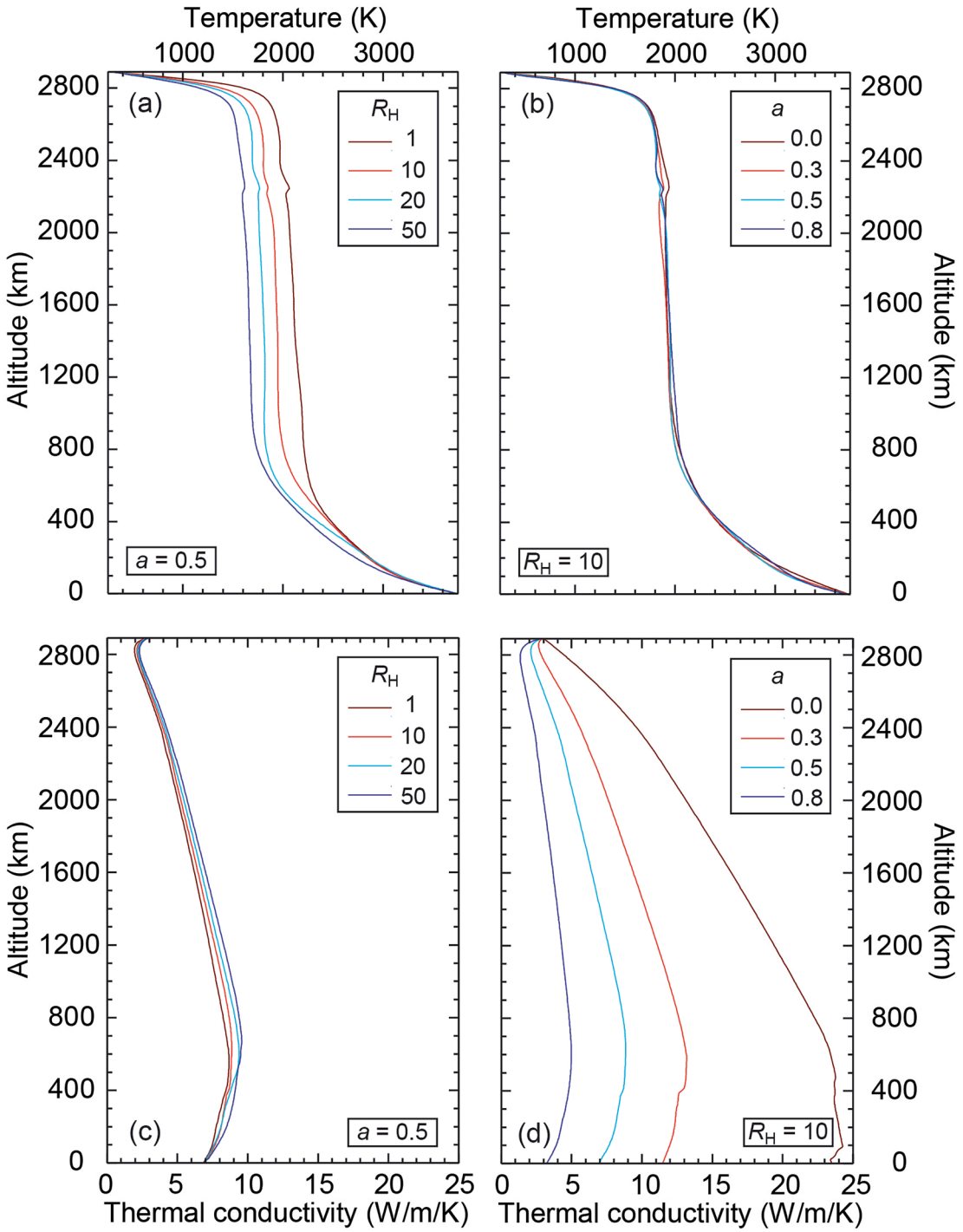

Extended Data Fig. 3 | Horizontally average profiles of temperature (a and b) and thermal conductivity (c and d) for selected cases. In panels (**a**) and (**c**), the exponent a, controlling the thermal conductivity temperature-dependence of thermal conductivity, is fixed to 0.5 and 4 values of the excess heating ratio in piles of dense material, R_H, are considered (legend). In panels (**b**) and (**d**), R_H is fixed to 10 and 4 values of a are considered (legend). All profiles correspond to snapshots taken at the end of each simulation.

https://doi.org/10.1038/s41561-026-02018-w

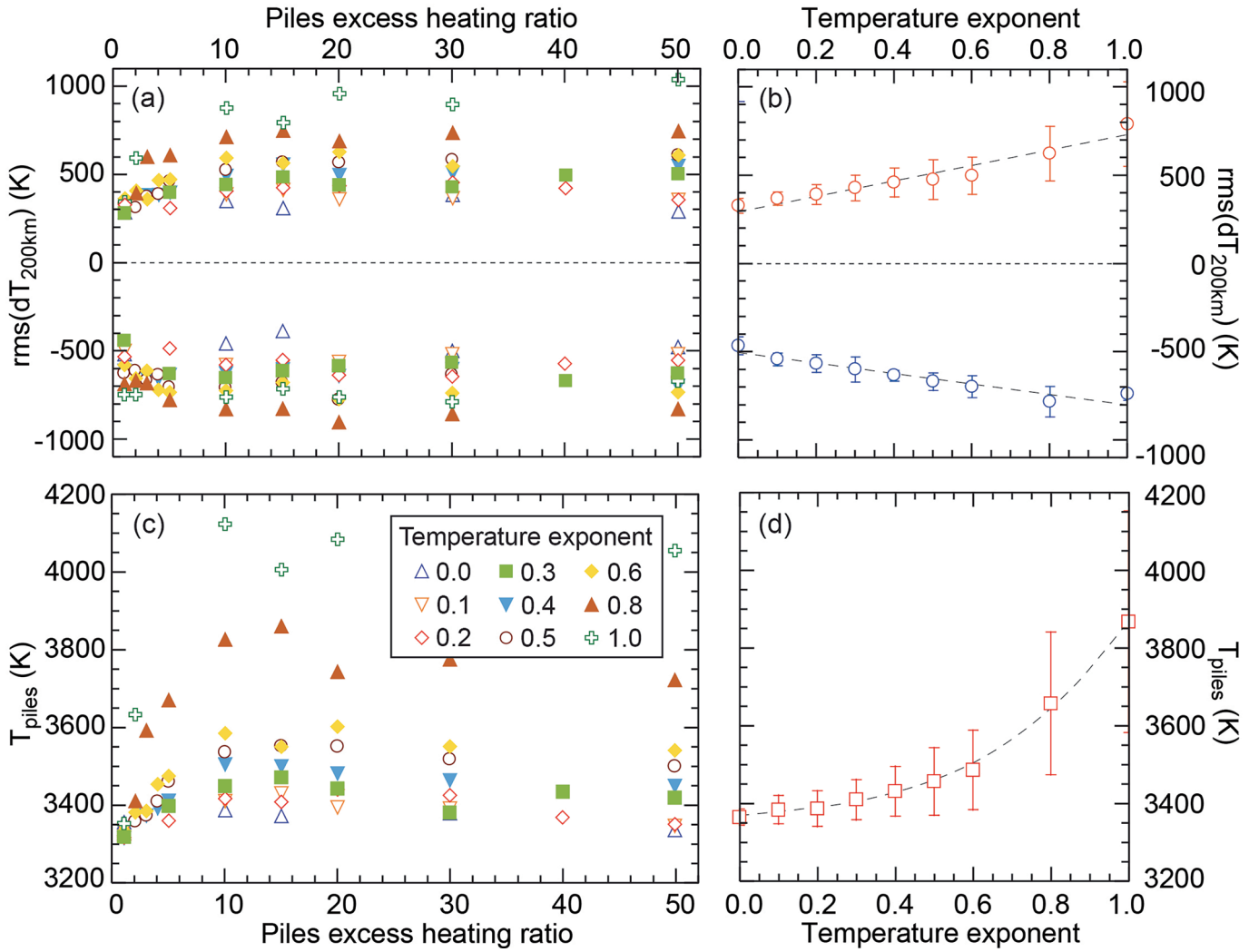

Extended Data Fig. 4 | Time-averaged core-mantle boundary temperature statistics. Data are averaged over the last 2 Gyr of simulations. (**a** and **b**) Root mean square of the positive and negative temperature anomalies in the lowermost 200 km (for convenience, the rms of negative anomalies are multiplied by a minus sign). (**c** and **d**) Average temperature of thermo-chemical piles. Panels (**a**) and (**c**) plot data as a function the piles excess heating ratio, R_H, and for several values of the temperature exponent of thermal conductivity, a, (color code). In panels (**b**) and (**d**), data are further averaged out over all the values of R_H (5 to 10 samples, depending on a), the error bars indicating one standard deviation, and represented as a function of the temperature exponent a.

https://doi.org/10.1038/s41561-026-02018-w

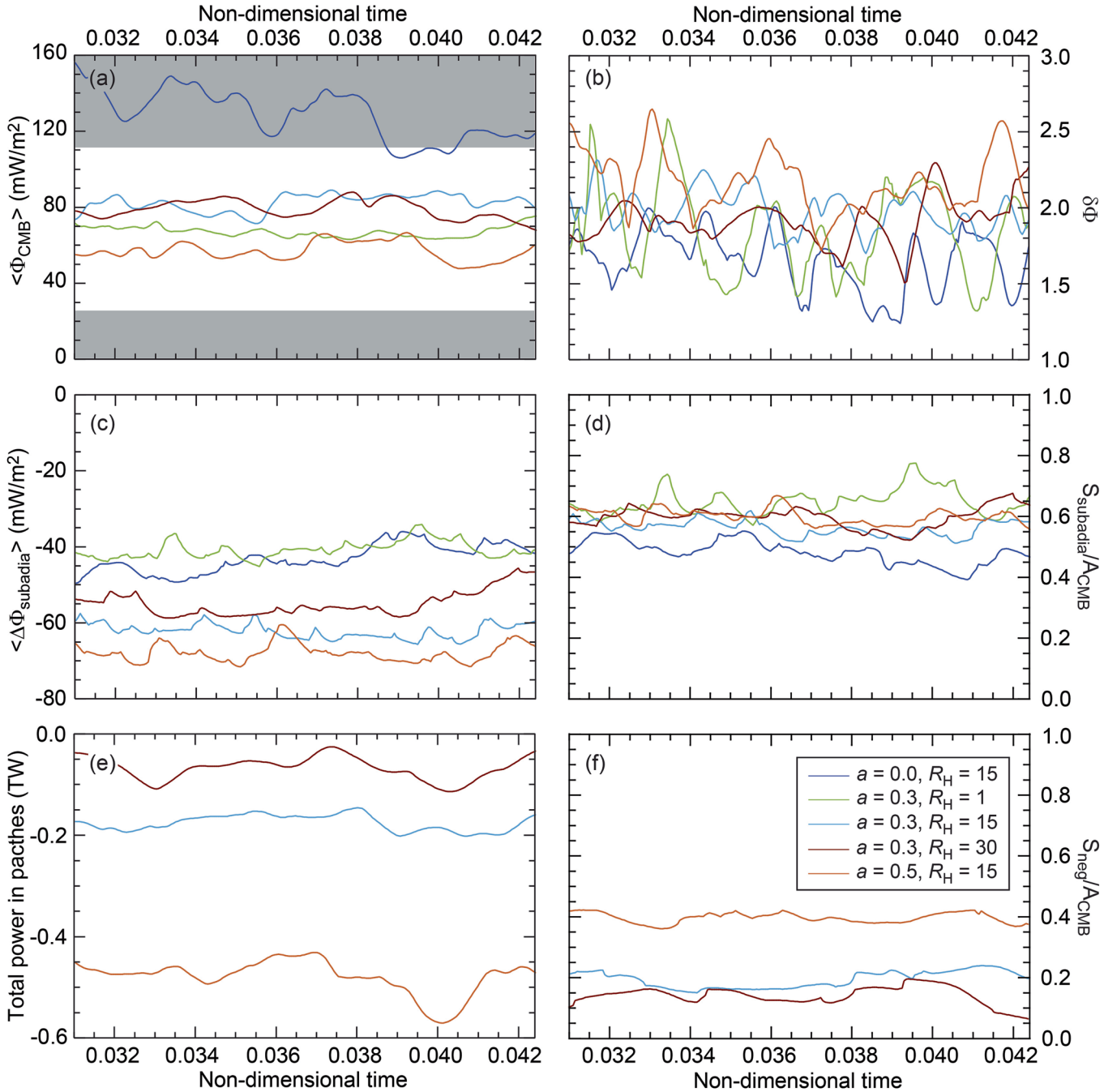

Extended Data Fig. 5 | Time variations in heat flux and related quantities for selected cases. Different combinations of the thermal conductivity temperature exponent, a, and of the excess heating ratio in piles of dense material, R_H, are considered. (**a**) average CMB heat flux, $<\Phi_{CMB}>$, (**b**) heat flux heterogeneity $\delta\Phi$ (see Methods for definition), (**c**) average residual subadiabatic heat flux, $<\Delta\Phi_{subadia}>$, defined as the difference between the average heat flux in subadiabatic regions and the core adiabatic heat flux, Φ^{core}_{adia} (here fixed to 70 mW/m^2), (**d**) surface fraction (with respect to the CMB area) of the subadiabatic regions, (**e**) total power in patches of negative heat flux, P_{neg}, and (**f**) surface fraction (with respect to the CMB area) of the negative heat flux regions. The grey shaded areas in panel (**a**) indicate the estimated CMB heat flux from ref. 36. The negative sign in panel (**e**) is imposed by convention to indicate that heat flows from the mantle to the core. The time axis is graduated in non-dimensional units, the whole duration being equivalent to 4 Gyr.

https://doi.org/10.1038/s41561-026-02018-w

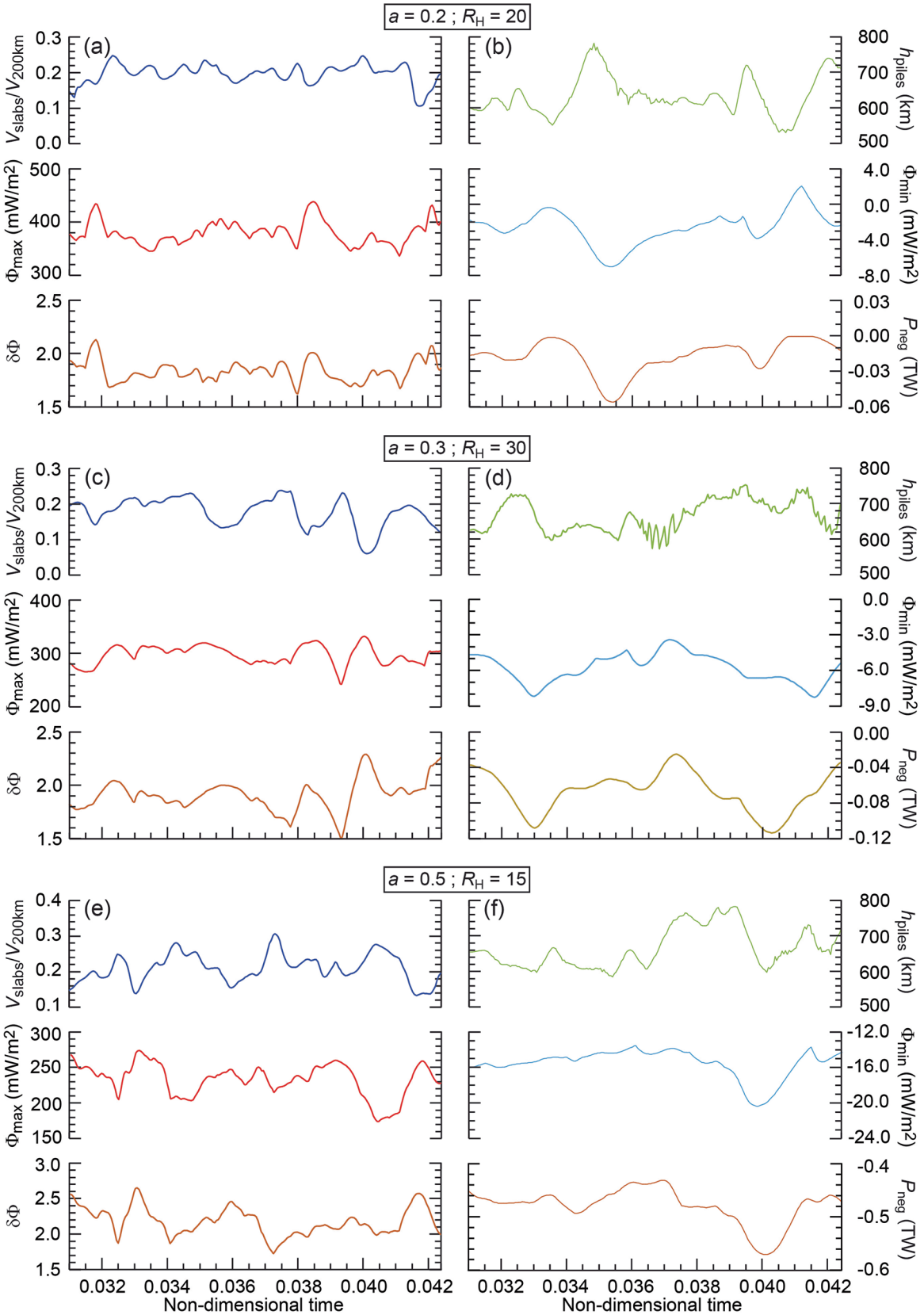

Extended Data Fig. 6 | Time variations of various properties for selected cases. Different combinations of the thermal conductivity temperature exponent, a, and of the excess heating ratio in piles of dense material, R_H, are considered. Left row (panels **a**, **c**, and **e**): slab volume fraction in the lowermost 200 km (top row of each panel), maximum CMB heat flux (middle row of each panel), and heat flux heterogeneity (bottom row of each panel). Right column (panels **b**, **d** and **f**): piles highest altitude (top row of each panel), minimum CMB heat flux (middle row of each panel) and total power in patches of negative CMB heat flux (bottom row of each panel). The negative sign in the patches power plots is imposed by convention to indicate that heat flows from the mantle to the core. The time axis is graduated in non-dimensional units, the whole duration being equivalent to 4 Gyr.

https://doi.org/10.1038/s41561-026-02018-w

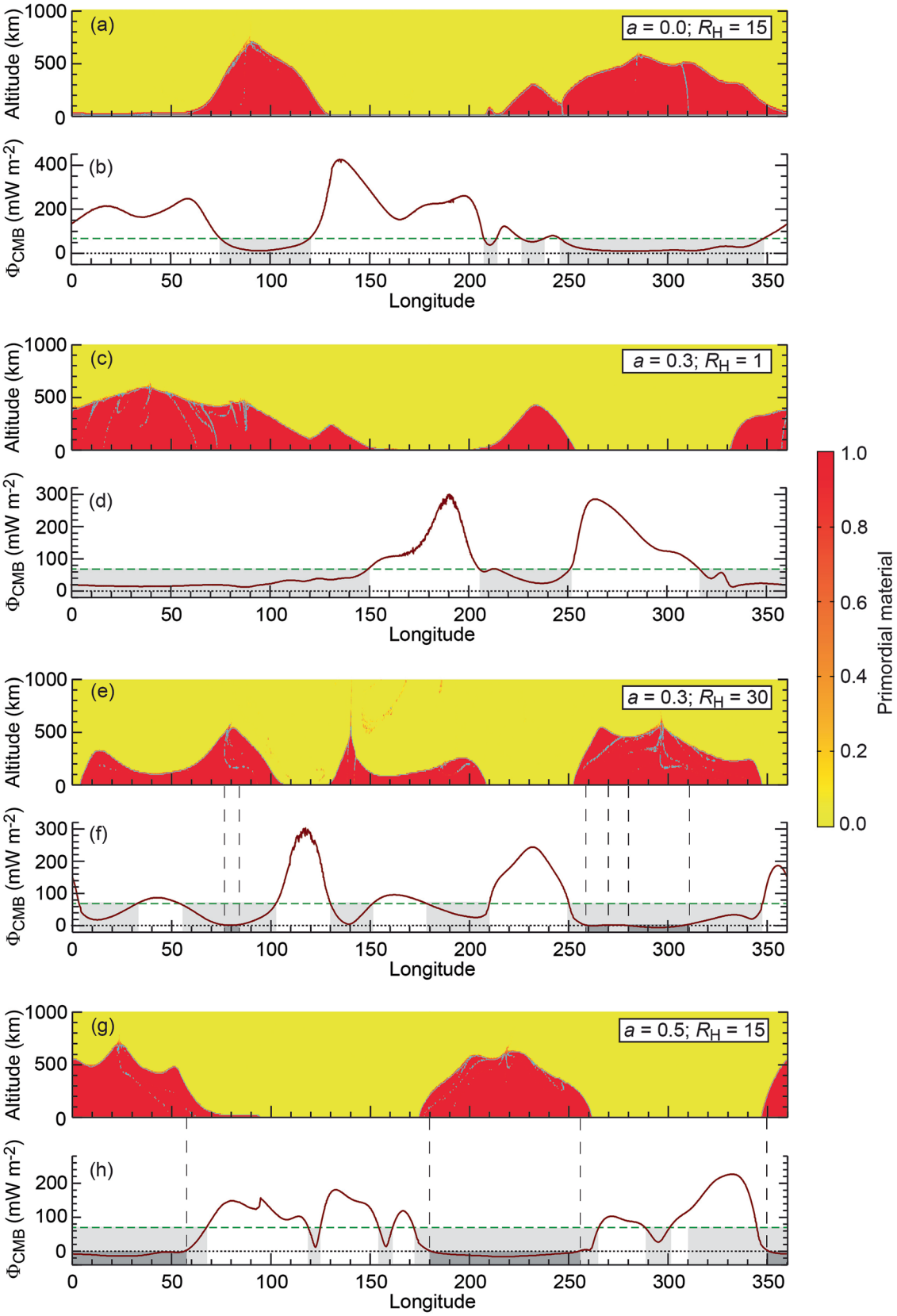

Extended Data Fig. 7 | Fraction of dense primordial material (color code) and core-mantle boundary heat flux as a function of longitude. a–h, Different combinations of piles excess heating ratio, R_H, and temperature exponents of thermal conductivity, a, are considered. Data were calculated on a spherical annulus and projected on a 2D-Cartesian grid. In panels showing C_{prim} the cyan contours indicate the composition isolines with an interval of 0.1. In panels showing the CMB heat flux, the green dashed line indicates the core adiabatic heat flux, Φ_{adia}^{core}, assuming an adiabatic gradient of 1 K/km and a core conductivity of 70 W m^{-1} K^{-1}, and the light and dark grey areas show the lateral extensions of regions with heat flux lower than Φ_{adia}^{core} and with negative heat flux, respectively.